JACS
JOURNAL OF THE AMERICAN CHEMICAL SOCIETY
pubs.acs.org/JACS
Article

Enhanced Cuprophilic Interactions in Crystalline Catalysts Facilitate the Highly Selective Electroreduction of CO_2 to CH_4

Lei Zhang,[+] Xiao-Xin Li,[+] Zhong-Ling Lang,[+] Yang Liu, Jiang Liu, Lin Yuan, Wan-Yue Lu, Yuan-Sheng Xia, Long-Zhang Dong, Da-Qiang Yuan, and Ya-Qian Lan*

Cite This: https://dx.doi.org/10.1021/jacs.0c11450

ABSTRACT: Cu(I)-based catalysts have proven to play an important role in the formation of specific hydrocarbon products from electrochemical carbon dioxide reduction reaction (CO_2RR). However, it is difficult to understand the effect of intrinsic cuprophilic interactions inside the Cu(I) catalysts on the electrocatalytic mechanism and performance. Herein, two stable copper(I)-based coordination polymer (**NNU-32** and **NNU-33(S)**) catalysts are synthesized and integrated into a CO_2 flow cell electrolyzer, which exhibited very high selectivity for electrocatalytic CO_2-to-CH_4 conversion due to clearly inherent intramolecular cuprophilic interactions. Substitution of hydroxyl radicals for sulfate radicals during the electrocatalytic process results in an in situ dynamic crystal structure transition from **NNU-33(S)** to **NNU-33(H)**, which further strengthens the cuprophilic interactions inside the catalyst structure. Consequently, **NNU-33(H)** with enhanced cuprophilic interactions shows an outstanding product (CH_4) selectivity of 82% at −0.9 V (vs reversible hydrogen electrode, j = 391 mA cm^{-2}), which represents the best crystalline catalyst for electrocatalytic CO_2-to-CH_4 conversion to date. Moreover, the detailed DFT calculations also prove that the cuprophilic interactions can effectively facilitate the electroreduction of CO_2 to CH_4 by decreasing the Gibbs free energy change of potential determining step ($*H_2COOH \rightarrow *OCH_2$). Significantly, this work first explored the effect of intrinsic cuprophilic interactions of Cu(I)-based catalysts on the electrocatalytic performance of CO_2RR and provides an important case study for designing more stable and efficient crystalline catalysts to reduce CO_2 to high-value carbon products.

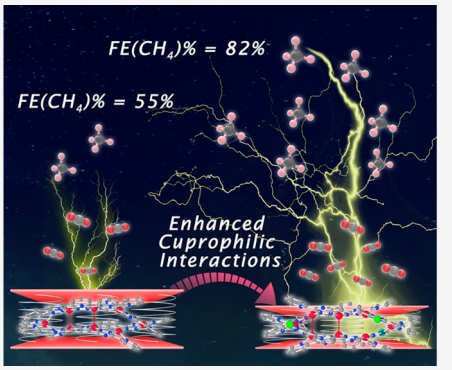

INTRODUCTION

Electrocatalytic reduction of CO_2 to highly valued fuels or chemicals has emerged as an important and efficient method, which is expected to reduce the concentration of carbon dioxide in the atmosphere and alleviate the energy crisis.[1−7] In particular, the highly selective electrocatalytic reduction of CO_2 to hydrocarbon fuels, such as methane and ethylene, has received enough attention recently, because these hydrocarbon products have been widely used in human life or industry and occupied a dominant position.[8−14] In recent years, Cu-based catalysts have been proved to have unique advantages in CO_2 electroreduction for they can reduce CO_2 to various products with high selectivity, including hydrocarbons, alcohols, etc.[15−21] However, there is still a lack of research on the main factors affecting the high selective conversion of CO_2 to specific products, which will greatly limit the design and synthesis of more advanced electrocatalysts. From the previous work, the effects of crystal face,[22] macroscopic morphology,[23] size,[24] valence state,[25,26] and other factors[27,28] of Cu-based catalysts on the activity and selectivity of CO_2RR have been carefully investigated. Especially, Cu(I)-based catalysts have received much attention for their outstanding performance on CO_2RR, which have studied the effect of grain boundaries on selectivity of products at present.[29,30] Nevertheless, it is very important but challenging to effectively stabilize the Cu(I) active site rather than be reduced to Cu(0) during the process of electrocatalytic CO_2RR. In this regard, recently, Sargent and co-workers constructed a series of boron-doped copper catalysts with stable oxidant state (∼+0.25 to +0.78) and realized outstanding stability for ∼40 h sustained CO_2RR to C_2 hydrocarbons.[31] Similarly, effectively stabilizing the Cu(I) active sites in Cu-based electrocatalysts would also have an important effect on the durable conversion of CO_2 to specific products, although it has not been reported so far. To our knowledge, the materials containing strong cuprophilic interactions (with Cu−Cu distance in the range of 2.4−3.0 Å) are beneficial to stabilize Cu(I) ions and enhance the electronic conductivity.[32,33] Thus, we think these materials with such advantages are proper candidates to construct

Received: October 31, 2020

electrocatalysts with stable Cu(I) catalytic sites and then study their impact on CO_2RR.

Coordination polymers are a kind of crystalline material composed of metal ions or clusters connected with organic ligands through coordination bonds whose well-defined single crystal structure can be accurate to the atomic level, and they are ideal catalyst models that can be designed and assembled reasonably according to specific structural requirements.[34−37] These materials can also provide accurate structural information for the identification of catalytic active sites and the study of a catalytic reaction mechanism.[38−41] In addition, assembling suitable metal ions and organic ligands can endow the compounds with excellent stability.[42−44] Based on the above, the coordination polymer materials have great advantages in the design of the specific structure of catalysts for electrocatalytic CO_2RR.[45−47] Therefore, in order to design and synthesize the above-mentioned catalysts with intramolecular cuprophilic interactions to study their effects on the electrocatalytic stability and performance, we hope to achieve this goal with the help of the structural designability of coordination polymers.

Taking into account the above considerations, two stable coordination polymers **NNU-32** and **NNU-33(S)** (S = sulfate radical) were constructed by a rigid nitrogen-containing polydentate chelating ligand 2-(5-(3-(5-(pyridin-2-yl)-1H-1,2,4-triazol-3-yl)phenyl)-1H-1,2,4-triazol-3-yl) pyridine (H_2bptb) and Cu(I) ions. **NNU-32** is an octanuclear Cu(I) cluster, and **NNU-33(S)** can be regarded as a two-dimensional compound with sql topology connected by **NNU-32** clusters (as subunits) and Cu (I) ions (as linkers). Both **NNU-32** and **NNU-33(S)** are crystallized with clear intramolecular cuprophilic interactions. We found that **NNU-32** can be stable in 1 M KOH solution while **NNU-33(S)** was transferred to **NNU-33(H)** (H = hydroxyl radical) with anion exchange, which was proved by PXRD, XPS analysis, and DFT calculation. When utilized **NNU-32** and **NNU-33(H)** as electrocatalysts, the products of CO_2RR were mainly CH_4 because of the contribution of cuprophilic interactions. The greatly enhanced cuprophilic interactions were observed in **NNU-33(H)** and endowed it with efficient performance of high selectivity for CO_2 to CH_4 electrocatalytic conversion with 82% faradic efficiency at −0.9 V vs RHE (j = 391 mA/cm^2), which showed one of the best performance among reported Cu-based catalysts for electrocatalytic CO_2 to CH_4 conversion. The in situ OH^- substitution for the inherent SO_4^{2-} in the molecule made **NNU-33(H)** have better adsorption capacity for CO_2 to further improve the CO_2RR performance. Importantly, the Cu(I) catalytic centers in **NNU-33(H)** were proved to be extremely stable under CO_2RR conditions by X-ray absorption spectroscopy (XAS), *in situ* Raman, X-ray photoelectron spectroscopy (XPS), and *in situ* Fourier transform infrared spectroscopy (FTIR) characterizations and thus an outstanding electrocatalytic stability on CO_2-to-CH_4 reduction for at least 5 h. Based on experimental results, DFT calculations were carried out to prove that cuprophilic interactions indeed play an essential role in the CO_2RR to CH_4 process for lowering the free energy of potential determining step (*H_2COOH → *OCH_2). It is worth noting that our study is the first case to achieve electrocatalytic CO_2-to-CH_4 conversion with such high selectivity catalyzed by coordination polymer catalysts with well-defined and stable structures and explore the role of cuprophilic interactions in electrochemical CO_2RR to a specific hydrocarbon product (CH_4).

RESULTS

Structure and Characterization of NNU-32 and NNU-33(S). Single crystal X-ray diffraction analysis revealed that **NNU-32** crystallizes in triclinic space group *P*-1 with an asymmetric unit consisting of two octanuclear copper clusters and one DMF molecule (Figure S1). Each cluster unit contains eight Cu ions and four bptb^{2-} ligands (Figure 1a). The

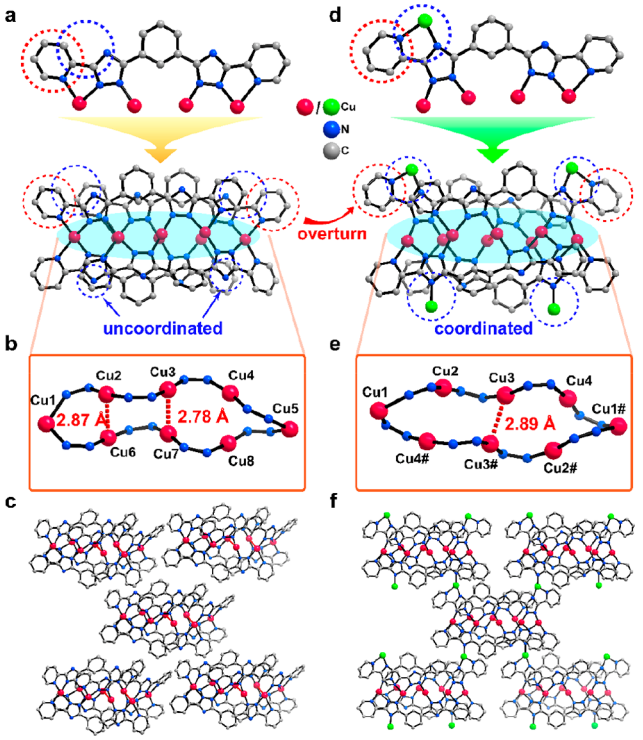

Figure 1. The crystal structures of **NNU-32** and **NNU-33(S)**: (a) structure of **NNU-32**, (b) coordination environment of Cu(I) ions in **NNU-32**, (c) arrangement of neighboring five {Cu_8} clusters, (d) subunit structure of **NNU-33(S)**, (e) coordination environment of Cu(I) ions in subunit of **NNU-33(S)**, and (f) {Cu_8} clusters connected with Cu(I) ions to form a single layer.

coordination environment of the four ligands is the same, of which two Cu ions are chelated by N from pyridine (dotted red circle in Figure 1a) and triazole, the other two Cu ions are coordinated with the adjacent nitrogen atom from triazole (Figure S2). All the N atoms in dotted blue circles are uncoordinated. The location of eight Cu ions in **NNU-32** forms an ellipse and two cuprophilic interactions (Cu_2−Cu_6 and Cu_4−Cu_8) can be found due to the short distance (<3.0 Å) between three pairs of opposite Cu ions (Figure 1b and Figure S3). Due to the lack of linkers, the {Cu_8} clusters are independent of each other (Figure 1c).

NNU-33(S) crystallizes in tetragonal space group $P4_12_12$ with an asymmetric unit containing five Cu ions, two deprotonated bptb^{2-} ligands, and 1/2 dissociative SO_4^{2-} ion (Figure S4). The subunit of **NNU-33(S)**, an octanuclear copper cluster, has a similar architecture with **NNU-32** (Figure 1d). The difference is that two of the terminal pyridine rings are overturned and chelated another Cu ion (dotted blue circles in Figure 1d and Figure S5) which coordinated with a N

https://dx.doi.org/10.1021/jacs.0c11450
J. Am. Chem. Soc. XXXX, XXX, XXX−XXX

atom from neighboring subunit. The coordination environment of Cu ions in the subunit of **NNU-33(S)** is almost the same as those in **NNU-32** except that Cu_1 and $Cu_{1\#}$ of **NNU-33(S)** corresponding to Cu_1 and Cu_5 in **NNU-32** are coordinated in CuN_3 environments rather than CuN_4 (Figure 1e and Figure S6). Cuprophilic interaction between Cu_3 and $Cu_{3\#}$ is determined for the appropriate distance (2.89 Å). Cu_5 in **NNU-33(S)** acts as a linker connecting two adjacent clusters coordinated with the pyridine N and two triazole in a triangular geometry, causing each subunit to connect with four other clusters to form a 2D layer (Figure 1f). Figure S7 shows the layer network stacking along the *a*, *b*, and *c*-axes. Besides, regarding the subunit cluster as a 4-connected node, the skeleton of **NNU-33(S)** features a topology with the Schläfli symbol of $4^4 \cdot 6^2$, which reveals the topology of the sql code (Figure S8). The oxidation states of all the Cu ions are calculated to be Cu(I) from their coordination environment, which suggest the 2D layers are cationic frameworks with SO_4^{2-} as counterions.

Chemical Stability of NNU-32 and NNU-33(S). Phase purity and chemical stability of **NNU-32** and **NNU-33(S)** were determined by analysis of powder X-ray diffraction (PXRD) patterns. The well-matched curves of simulated, experimental and after soaking **NNU-32** sample in 1 M KOH solution suggested that **NNU-32** can maintain its structure in alkaline conditions (Figure S9). Nevertheless, when leaving **NNU-33(S)** in 1 M KOH solution, some of the peaks of PXRD patterns were changed from the original curve over time (Figure 2a). It can be found that the peak originally located in 10.46° gradually shifted to the left along with the weakening of intensity and eventually disappearing after 24 h. Simultaneously, a new peak near 11° sprouted and the intensity kept increasing. The location of new peak was shifting to right slightly and finally ended at 11.24°. On the range of ~24−30°, two peaks at 26.88° and 27.58° were gradually fading and disappearing accompanied by a new peak arising at 26.01°. All the changes of PXRD patterns indicated the structure of **NNU-33(S)** had changed slightly and continually in 1 M KOH solution, while the generally similar curves can prove that the framework of **NNU-33(S)** was not dissociated. In order to get the final skeleton, we soaked **NNU-33(S)** single crystals in 1 M KOH and analyzed the crystal structure by single-crystal X-ray diffraction (SCXRD). SCXRD analysis revealed that single-crystal-to-single-crystal transformation indeed happened from **NNU-33(S)** to **NNU-33(I)** (I = intermediate state). The reason for calling it an intermediate state is that the simulated PXRD pattern of **NNU-33(I)** still has a slight difference to that after soaking in KOH solution (Figure S10). Furthermore, based on the initial structure of **NNU-33(I)**, a refined model **NNU-33(H)** (H = hydroxyl) was obtained using density functional theory (DFT) by Materials Studio 9.0 version (*DMol*^{3} program). Le Bail fitting on the PXRD pattern using the EXPO-2014 program with R_w and R_{wp} values of 2.803% and 3.742% are evidence of the reliability of the computation result (Figure 2b). PXRD patterns compared the simulated and experimental **NNU-33(S)**, **NNU-33(S)** after soaking in 1 M KOH, and simulated **NNU-33(H)** suggested the structure of **NNU-33(H)** is more reasonable to the real configuration. **NNU-33(H)** assumes the space group of $P4_12_12$ with $a = b =$ 16.3355 Å, c = 31.5523 Å, and $\alpha = \beta = \gamma = 90°$. Compared with the original structure **NNU-33(S)**, the subunit $\{Cu_8\}$ cluster is more compressed. The height of the cluster was reduced from 7.77 to 6.72 Å (Figure 2c,d), resulting in the distance between

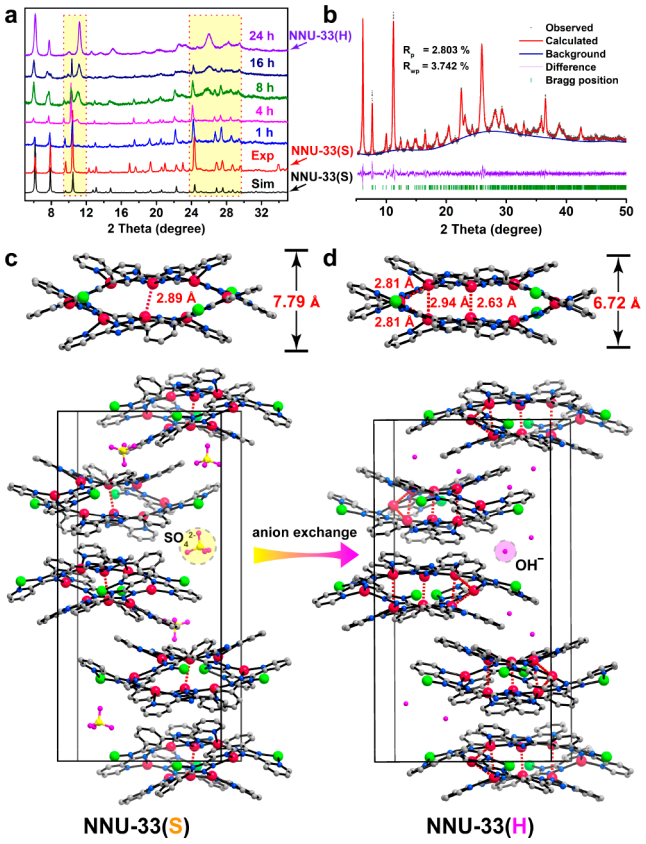

Figure 2. Dynamic transition of catalyst structure from **NNU-33(S)** to **NNU-33(H)**: (a) PXRD patterns of soaking NNU-33(S) in 1 M KOH solution at different times, (b) PXRD patterns of simulated and observed **NNU-33(H)**, and (c and d) structures of $\{Cu_8\}$ clusters and unit cell in **NNU-33(S)** and **NNU-33(H)**, respectively.

the middle pair of Cu ions ($Cu_3-Cu_{3\#}$) decreasing from 2.89 to 2.63 Å (Figures S11−S14). In addition, the distances of Cu_1-Cu_2, $Cu_1-Cu_{2\#}$, and $Cu_2-Cu_{2\#}$ are all close to less than 3 Å (2.81 Å, 2.81 Å, and 2.94 Å, respectively), which indicates the enhanced cuprophilic interactions in **NNU-33(H)** than **NNU-33(S)**. From the view of the unit cell, the original SO_4^{2-} ions were exchanged with OH^- (Figure 2c,d). In contrast to **NNU-33(I)** ($a = b$ = 16.441 Å, c = 31.090 Å), the length of the *c* axis of **NNU-33(H)** shows an increase (Table S4). It indicates that the basal spacing of **NNU-33(H)** is wider than **NNU-33(I)** and suggests that the interlayer distances of **NNU-33(H)** are expanded along with structural transformation, which might result in more CO_2 adsorption and catalytic sites explosion during the electrochemical CO_2RR progress.

Performance of Electrocatalytic CO_2 Reduction. Both **NNU-32** and **NNU-33(H)** can keep stable in 1 M KOH solution, so we utilized them as electrode materials and tested their performance of CO_2RR. All electrochemical tests were evaluated in a custom three-channel flow cell. The Faradaic efficiency (FE) of electrocatalytic gaseous products were evaluated by gas chromatography (GC), and the liquid products were evaluated by nuclear magnetic resonance (NMR) and ion chromatography (IC). Before CO_2RR electrochemical experiments were carried out, linear sweep voltammetry (LSV) curves of **NNU-32** and **NNU-33(H)** were measured under CO_2 and Ar streams, respectively, across 1 M KOH interface at a wide potential range from −0.5 V to −1.0 V (vs RHE, all the following potentials are on the RHE scale).

https://dx.doi.org/10.1021/jacs.0c11450
J. Am. Chem. Soc. XXXX, XXX, XXX−XXX

As shown in Figure S17, both of the two samples delivered higher current densities and lower onset potential in CO_2 flow than that in Ar, suggesting the possibility of CO_2 electroreduction. Meanwhile, the current density of **NNU-33(H)** was always higher than that of **NNU-32**, which revealed that **NNU-33(H)** has higher activity for the CO_2RR. Then the current outlines along with **NNU-32** and **NNU-33(H)** under the fairly wide range of potentials were measured and shown in Figure S18. It revealed that both of **NNU-32** and **NNU-33(H)** can maintain a stable current from −0.5 V to −1.0 V. Compared with **NNU-32** constituted by isolated clusters, **NNU-33(H)** with a two-dimensional framework showed higher current densities at each potential, signifying that **NNU-33(H)** is more conducive for electron transfer. Moreover, the values of electrochemical double-layer capacitance (C_{dl}) were calculated from cyclic voltammograms (CV) curves to evaluate the electrochemical active surface area (ECSA) of **NNU-32** and **NNU-33(H)**.[48] The C_{dl} value of **NNU-33(H)** was calculated to be 3.94 mF cm^{-2}, which is much higher than that of **NNU-32** (2.47 mF cm^{-2}) (Figures S19 and 20). It suggested that **NNU-33(H)** can provide more catalytic sites to contact the electrolyte, leading to increase the reaction speed during the electrocatalytic process.

The electrochemical reduction of CO_2 performance in **NNU-32** and **NNU-33(H)** was measured in 1 M KOH aqueous electrolyte (the detailed values of faradic efficiency of each product using **NNU-32** and **NNU-33(H)** as electrocatalysts are listed in Tables S6 and S7, respectively). As shown in Figure S21a, as for the catalytic selectivity toward the formation of different products over **NNU-32** samples, the CO_2 electroreduction experiments were performed at different potentials (∼−0.5 to −1.0 V), and the corresponding product distribution is illustrated. It revealed that the products were mainly H_2, CO, CH_4, and C_2H_4, while the FE_{HCOO^-} were below 2% at all potentials (Table S6). **NNU-32** gave the highest FE_{CO} (44.46%) at −0.5 V and with a current density of 28.54 mA cm^{-2}, along with a FE_{H2} of 50.78%. Little amounts of CH_4 (1.14%), C_2H_4 (3.92%), and $HCOO^-$ (0.88%) were also detected. When the potentials increased to −0.6 V (j = 32.07 mA cm^{-2}) and −0.7 V (j = 47.83 mA cm^{-2}), the FE_{H2} were decreased to 45.72% and 35.21%, respectively. Also, the FE_{CO} were decreased to 42.02% (−0.6 V) and 33.53% (−0.7 V), which showed that H_2 and CO were the main products at applied potentials of ≤−0.7 V. Nonetheless, the FE_{CH4} and FE_{C2H4} kept increasing from 1.14% to 23.11% and 3.92% to 6.16% with the applied potentials increasing from −0.5 V to −0.7 V. As the potential applied to higher than −0.8 V, the main electroreduction products tended to be CH_4. It exhibited the highest FE_{CH4} that was 55.1% at −1.0 V (j = 384.16 mA cm^{-2}), and the corresponding FE_{CO} was decreased to 1.57% with a FE_{H2} of 40.41%. The FE_{HER}, FE_{CO2RR}, and FE_{CH4} at each potential are summarized in Figure S21b. The faradic efficiency of hydrogen as the competitive product along with **NNU-32** as the electrocatalyst were above 30% at all the potentials from −0.5 V to −1.0 V. The highest FE_{CO2RR} was 63.93% at −0.8 V. It can be found when the potential exceeded −0.7 V, CH_4 was the main product of CO_2RR.

In contrast, when the catalyst was changed into **NNU-33(H)**, as shown in Figure 3a, under the same sample density of 1 mg cm^{-2}, CO was also the primary reduction product with FE values of about 64.46% and 58.41% along with FE_{H2} of 30.78% and 29.32% at potentials at −0.5 V (j = 60.58 mA cm^{-2}) and −0.6 V (j = 102.67 mA cm^{-2}), respectively. The

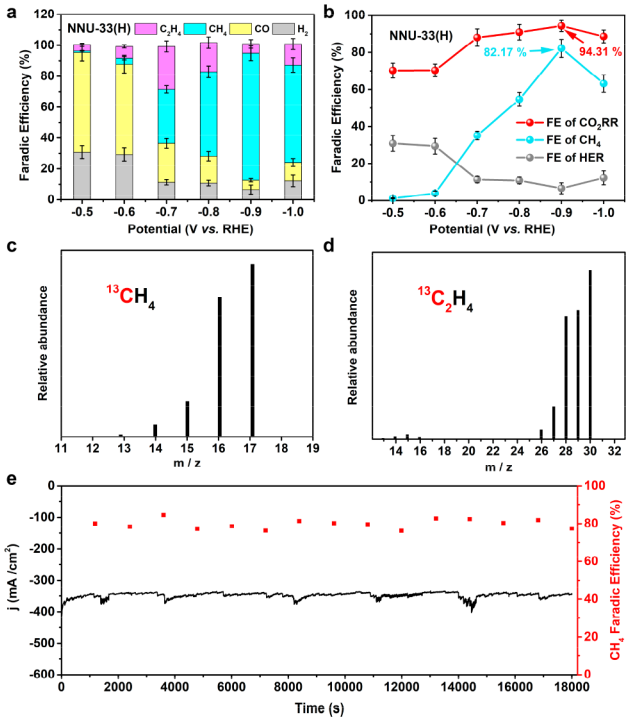

Figure 3. Electrocatalytic performances of **NNU-33(H)**: (a) faradaic efficiency (FE) of H_2, CO, CH_4, and C_2H_4 products with **NNU-33(H)** as electrocatalyst; (b) comparison of FE for HER, total CO_2RR, and CH_4 conversion catalyzed by **NNU-33(H)**; (c and d) mass spectra extracted from GC-MS analysis of CH_4 and C_2H_4 product from $^{13}CO_2$ reduction; (e) current profile and FEs of CH_4 at a constant voltage of −0.9 V vs RHE.

faradic efficiencies of CH_4 and C_2H_4 were all less than 8%. Specifically, **NNU-33(H)** gave the highest FE_{C2H4} value (27.71%) at −0.7 V (j = 176.08 mA cm^{-2}). The FE_{H2} and FE_{CO} decreased to 11.34% and 25.1% with FE_{CH4} increasing to 35.1%. With the potential continuously increasing, CH_4 became the dominant competitive advantage over other carbon products evolution. Only 6.58% of FE_{H2}, 6.1% FE_{CO}, and 6.04% of FE_{C2H4} were detected at −0.9 V. The highest FE_{CH4} was determined to be 82.17 (j = 391.79 mA cm^{-2}), and the total FE_{CO2RR} was up to 94.31% (Figure 3b), which is the first case to achieve electrochemical CO_2RR to CH_4 with such high selectivity along with a coordination polymer as the catalyst and shows the one of the best performances of electroreduction from CO_2 to CH_4 among Cu-based catalysts[8,9,22,23,29,49−53] (Table S8). When the applied potential reached to −1.0 V, the FE_{CH4} was reduced to 63.19% while the FE_{H2} increased to 12.24%, which suggested the most appropriate applied potential of **NNU-33(H)** is −0.9 V. In addition, the FE_{HCOO^-} remained below 1% at the applied potentials from −0.5 V to −0.7 V and less than 0.01% at ∼−0.8 V to −1 V (Table S7). It is worth noting that the FE_{CO2RR} values of **NNU-33(H)** kept above 69% and higher than those of **NNU-32** at all the potentials from −0.5 V to −1.0 V. Importantly, isotope labeling experiment conducted under a $^{13}CO_2$ atmosphere revealed that all the carbon products were converted from CO_2 (Figure 3c,d and Figure S24). Catalytic stability for selective CO_2 reduction (into CH_4) was also evaluated in Figure 3e through monitoring variations in FE_{CH4} at intervals. The current density of **NNU-33(H)** maintained stable approximately j = 350 mA cm^{-2} and FE_{CH4}

https://dx.doi.org/10.1021/jacs.0c11450
J. Am. Chem. Soc. XXXX, XXX, XXX−XXX

values kept at about 75% all along in 5 h of continuous electroconversion at −0.9 V by detecting CH_4 every 20 min. It demonstrated that **NNU-33(H)** can keep both the activity and selectivity during the CO_2 reduction process.

DISCUSSION

It can be concluded from the above test performance that CH_4 was the main components of electrocatalytic CO_2RR along with **NNU-32** (55.1%/58.7%, FE_{CH4}/FE_{CO2RR} at −1.0 V) and **NNU-33(S)** (82.17%/94.31%, FE_{CH4}/FE_{CO2RR} at −0.9 V) as electrocatalysts. The excellent performance of CO_2-to-CH_4 conversion caught our attention. Through comparison, the PXRD patterns before and after the test, it can be found that **NNU-32** could maintain its structure and **NNU-33(S)** indeed converted into **NNU-33(H)** (Figures S25 and S26). It is worth noting that no obvious peak corresponding to Cu(0), Cu_2O, or CuO can be observed, which suggests the structure of catalysts can remain unchanged during the electrocatalytic process. The test of catalytic stability above revealed that **NNU-33(H)** was the real catalyst in CO_2RR. In order to further investigate the structural stability of these electrocatalysts and the oxidation state of Cu(I) catalytic center during the CO2RR process, XAS, *in situ* Raman, XPS, and *in situ* FTIR were performed. According to the results of Cu K-edge X-ray absorption near-edge structure (XANES) and corresponding absorption edge changes of **NNU-33(H)** before and after CO_2RR catalysis, the oxidant state of Cu(I) in **NNU-33(H)** was found to be unchanged, which indicated that the Cu(I) centers were not reduced to Cu(0) particles or turned into Cu_2O or CuO (Figure 4a,b).[31] The stable Cu(I) oxidant state was also proved by the unchanged Cu LM2 XPS spectra before and after CO_2RR under ∼−0.5 to −1 V (vs RHE) (Figure S25). Furthermore, *in situ* Raman spectroscopy was examined on **NNU-33(H)** before and during the CO_2RR process at different applied potentials (∼−0.5 V to −1 V vs RHE) to demonstrate the structural stability and track whether there

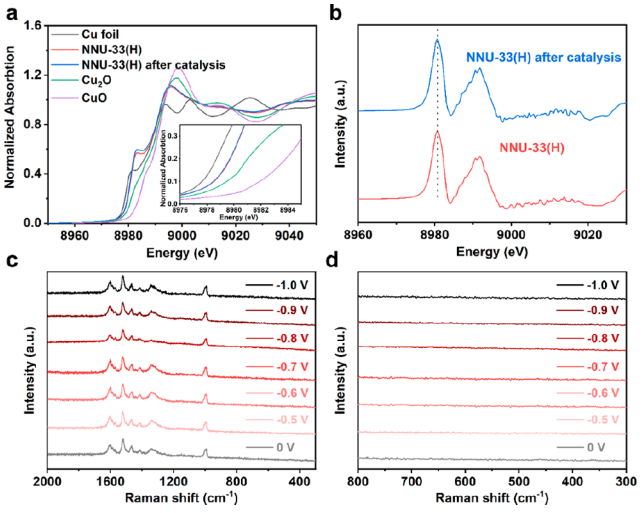

Figure 4. Stability of **NNU-33(H)** during the CO2RR process: (a) Cu K-edge XANES spectra of **NNU-33(H)** before and after CO_2RR catalysis, (b) absorption edge changes of **NNU-33(H)** before and after CO_2RR catalysis. The curves were determined by the first derivatives of the Cu K-edge XANES spectra, (c) *in situ* Raman spectra from 300 to 2000 cm^{-1} before and under CO_2RR potentials, and (d) magnified *in situ* Raman spectra from 300 to 800 cm^{-1} to detect the formation of Cu_2O or CuO.

was any Cu_2O or CuO generated on the surface of electrocatalysts. The unvaried Raman spectra before and under CO_2RR conditions suggested that **NNU-33(H)** can keep stable during CO_2RR (Figure 4c).[54] No peaks appeared in the range of 300−800 cm^{-1} indicated that no Cu_2O or CuO produced on the surface of **NNU-33(H)** under the reaction potentials (Figure 4d).[55,56] In addition, the stability of electrocatalyst was also proved by *in situ* FTIR (Figure S26). All the evidence indicated that the structures and Cu(I) oxidant state of electrocatalysts could keep stable under the CO_2 reduction conditions. Moreover, theoretical results, based on thermodynamic calculations and dynamic simulations, indicate the high stability of $\{Cu_8\}$ stems from the strong coordination of Cu(I) sites, including the Cu−N bonding and the cuprophilic interaction between the opposite Cu(I) ions, which prevent the dissociation of catalysts and formation of Cu clusters under electroreduction conditions (Figures S27−S30 and Movie S1).

From the structure analysis, the catalytic sites between **NNU-32** and **NNU-33(H)** are almost the same to be the three pairs of Cu(I) in the middle of $\{Cu_8\}$ clusters (Cu_2−Cu_6, Cu_3−Cu_7, and Cu_4−Cu_8 in **NNU-32** and Cu_2−$Cu_{2\#}$, Cu_3−$Cu_{3\#}$, and Cu_4−$Cu_{4\#}$ in **NNU-33(H)**) due to the steric hindrance of the rest of the Cu ions (Cu_1 and Cu_5) to the attack of CO_2. We found that both the valence (+1) and coordination environments of the corresponding catalytic sites in **NNU-32** and **NNU-33(H)** are nearly identical (Figure 1b and Figure S14c) except the difference of cuprophilic interactions, which may be the core to explain the high selectivity of CH_4 product. In **NNU-32**, only two cuprophilic interactions are determined and measured as 2.87 and 2.78 Å. While in **NNU-33(H)**, because of the deformation of $\{Cu_8\}$ cluster subunits, four cuprophilic interactions are measured as 2.81 Å, 2.81 Å, 2.94 Å, and 2.63 Å (4.06 Å, 3.70 Å, 2.87 Å, and 2.78 Å at the same location in **NNU-32**, respectively). Not only has the number of cuprophilic interactions doubled, it should be noted that the distances of Cu ions shorten obviously, which suggests the cuprophilic interactions in **NNU-33(H)** are more enhanced than **NNU-32**. Combined with the faradic efficiency of CH_4 during electrocatalytic CO_2RR of **NNU-32** (55.1%) and **NNU-33(H)** (82.17%), a rough positive correlation between FE_{CH4} and cuprophilic interactions is assumed: the existence of cuprophilic interactions can promote the conversion of CH_4, and the more the quantity and the shorter the distance, the more CH_4 can be produced.

On the other hand, to prove the anion exchange from SO_4^{2-} to OH^- during CO_2RR process in 1 M KOH solution, X-ray photoelectron spectroscopy (XPS) analyses were carried out to detect sulfur content in **NNU-33(S)** and **NNU-33(H)** (Figure S31). A peak located at 167.9 eV is corresponding to S of SO_4^{2-} in the obtained original structure, while it almost disappeared in **NNU-33(H)** suggesting only a trace S content remained in the skeleton. Furthermore, Fourier transform infrared spectroscopy (FTIR) characterization of **NNU-33(S)** soaking in 1 M KOH aqueous solution for different times was measured (Figure S32). It was shown that the IR asymmetric stretching vibration of SO_4^{2-} of **NNU-33(S)** at 1140 cm^{-1} gradually disappeared over time, and no distinct peak could be found after 32 h. This evidence can prove that SO_4^{2-} in **NNU-33(S)** can be substituted by OH^- in alkaline conditions by electrification. Because the volume of OH^- is smaller than the outgoing SO_4^{2-}, the distance between the two adjacent layers shrinks from 8.438 to 7.773 Å. Nonetheless, combined with

https://dx.doi.org/10.1021/jacs.0c11450
J. Am. Chem. Soc. XXXX, XXX, XXX−XXX

changes in the skeleton, the void volume of **NNU-33(H)** becomes larger than **NNU-33(S)** due to the formation of narrow pores along the *a* and *b* axes. PLATON analysis revealed that the free volume proportion of **NNU-33(H)** is 17.4% (1459.7 Å^3 out of the 8404.0 Å^3 unit cell volume), which can facilitate rapid gas transport across the electrode−electrolyte interface at high current densities. In addition, due to the hydroxide being introduced, **NNU-33(H)** displays a far greater performance on CO_2 adsorption (26.918 cm^3 g^{-1}) than original **NNU-33(S)** (4.249 cm^3 g^{-1}) and **NNU-32** (3.081 cm^3 g^{-1}) at 298 K (Figures S33 and S34), which is more conducive to CO_2RR.

DFT CALCULATIONS

In both **NNU-32** and **NNU-33(H)**, the up−down Cu(I)−Cu(I) distances located in a range of 2.78−2.94 Å, which are a little larger than twice the covalent radius of Cu (2.34 Å) but significantly shorter than twice its van der Waals radius (5.76 Å). This suggests a cuprophilic interaction may exist in the crystal, which may induce a remarkable influence on its catalytic activity and efficiency. To characterize the nature of those Cu(I)−Cu(I) interactions and reveal their role in the catalytic process, topological analysis of the electron density within the quantum theory of atoms in molecules (QTAIM) was performed for a {Cu_8} cluster model at the M06/6-31G**(C, N, O, H) and LANL2D(Cu)/PCM levels.[57−61] This theory establishes that a chemical bond exists if a line of a locally maximum electron density links two neighboring atoms and also if along that line there is a bond critical point (BCP). As the green ball representation in Figure 5a, all the intuitively

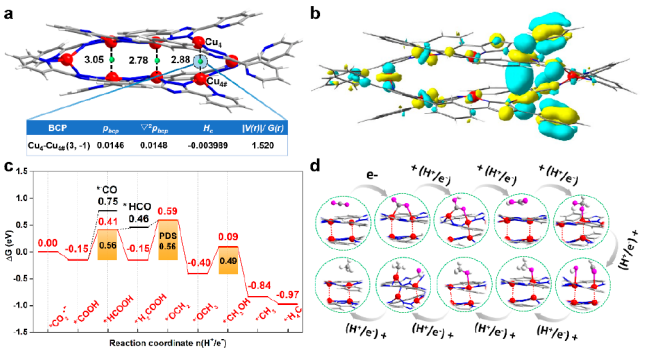

Figure 5. Cu(I)−Cu(I) bond interaction and DFT computed CO_2RR energy profile: (a) side view of the DFT optimized {Cu_8} cluster model taken from **NNU-33(H)** and the corresponding Cu(I)−Cu(I) distances (Å); bond critical points (BCP) are labeled in green; electron densities ρ [e Å^{-3}], its Laplacian $\nabla^2\rho$ [e Å^{-5}], total energy density (H_c), and $|V(r)|/G(r)$ ratio at the BCP between Cu_4 and $Cu_{4\#}$. (b) Relevant molecular orbitals involved in the Cu_4−$Cu_{4\#}$ interaction. (c and d) Calculated free energy diagram and the corresponding intermediates for CO_2 electrocatalytic reduction to CH_4 on the Cu_8 model catalyst.

expected bonds between the up and down Cu(I) ions are characterized by such BCPs. However, the electron density (ρ) at the BCP between Cu_4 and $Cu_{4\#}$ is 0.0146 e Å^{-3} (taking Cu_4−$Cu_{4\#}$ as an example), significantly lower than a general covalent-bond, such as C−C (1.698 e Å^{-3}). A comprehensive evaluation of $\nabla^2\rho_{bcp} > 0$, $H_c < 0$, and $1 < |V(r)|/G(r) < 2$ at this BCP indicates the Cu4−Cu4# interaction is an "intermediate interaction" that should be termed as partially covalent and partially electrostatic. In addition, the molecular orbital character by overlapping of Cu ($3d_z$) and Cu ($3d_z$) orbitals shown in Figure 5b also emphasized the donation nature of the Cu−Cu bond.

After confirming the Cu(I)−Cu(I) interactions in the crystal, we then paid attention to the detailed pathways for CO_2 reduction to reflect the role of the Cu−Cu interaction in the electrocatalytic procedure. Under electrochemical condition, CO_2 is generally fixed and was reduced stepwise to different products depending on the nature of the catalysts. As seen in Figure 5c,d, the dominant intermediates and energies involved in each elementary step are summarized. The $*CO_2$ precursor is preferred to form on the Cu(I) with adsorption free energy of 0.27 eV in a line mode. The first elementary step of CO_2RR is the hydrogenation of CO_2 by adding of a proton and extracting an electron from the electrode to form *COOH (* indicates the catalyst surface). However, this process is calculated to experience an extreme high energy of ∼1.00 eV, which may lead the rest steps to stand in a high energy level. Instead, the CO_2 could experience an electron transfer initially to form the $*CO_2^{\bullet-}$ anion radical, and the originally linear structure of CO_2 is regulated into a bent mode. Once $CO_2^{\bullet-}$ is formed, the subsequent H^+/e^- addition to form $COOH^{\bullet}$* is thermodynamic with much feasibility with the Gibbs free energy change of −0.15 eV and significantly more promoted than the direct H^+/e^- addition on CO_2 mediated by the preliminary catalyst. The second H^+/e^- hydrogenation occurred alternatively on O and C of *COOH to form *HCOOH and *CO, respectively. The formation of *HCOOH (0.56 eV) is thermodynamically easier than CO* (0.90 eV), supporting a relatively less selectivity for formation of CO. The *HCOOH intermediate is then further stepwise reduced to $*H_2COOH$, $*OCH_2$, $*OCH_3$, $*CH_3OH$, $*CH_3$, and $*CH_4$ with a corresponding free energy change of −0.55, 0.74, − 0.99, 0.49, − 0.93, and −0.13 eV. Looking at the overall reaction network, we can obtain the fourth hydrogenation step, namely, $*H_2COOH \rightarrow *OCH_2$, suffering the highest free energy change step (ΔG = 0.74 eV). In other words, this step is recognized as the potential determining step (PDS) for CO_2RR to generate CH_4 on the **NNU-32** and **NNU-33(H)**. However, the PDS process is significantly limited (ΔG = 1.11 eV) when we removed the Cu(I)−Cu(I) interaction by taking half of the model into account (Figure S35). This result confirms that the internal Cu−Cu interaction plays an essential role in the CO_2RR process.

CONCLUSION

In summary, we have synthesized two stable Cu(I)-based coordination polymer electrocatalysts (**NNU-32** and **NNU-33(H)**) with cuprophilic interactions and explored their performance of electrocatalytic CO_2RR in a flow-cell electrolyzer, which showed excellent abilities of CO_2-to-CH_4 conversion with high selectivity (82% at −0.9 V vs RHE catalyzed by **NNU-33(H)**) due to the existence of cuprophilic interactions. Because of the in situ dynamic crystal structure transition from **NNU-33(S)** to **NNU-33(H)** with substitution of hydroxyl radicals for sulfate radicals, it led to obviously enhanced cuprophilic interactions and the ability of CO_2 adsorption of **NNU-33(H)**, which resulted in such outstanding performance of selective CO_2-to-CH_4 electrocatalysis together. The systematic study of **NNU-32** and **NNU-33(H)** revealed that cuprophilic interactions played a crucial role for the generation of CH_4, and the selectivity of CH_4 depends on the quantity and distance of cuprophilic interactions. Briefly,

https://dx.doi.org/10.1021/jacs.0c11450
J. Am. Chem. Soc. XXXX, XXX, XXX−XXX

cuprophilic interactions endow the electrocatalysts with the ability to catalyze CO_2 to CH_4 selectively, and more quantities of cuprophilic interactions and shorter Cu(I)−Cu(I) distance can improve the selectivity of CH_4 formation. Specially, DFT calculation proved that the inherent cuprophilic interactions reliably accelerate the conversion efficiency of CO_2 to CH_4 by decreasing the free energy of potential determining step ($*H_2COOH \rightarrow *OCH_2$) for CO_2RR to generate CH_4. It is also important that the stable Cu(I) active sites endowed **NNU-33(H)** with good catalytic durability for at least 5 h. This work is the first time to discover the effect of the important structural information in Cu(I)-based catalysts on the selective CO_2-to-CH_4 conversion in electrocatalytic CO_2RR and establish an apparent and concrete structure−property relationship of cuprophilic interactions and electroreduction of CO_2 to CH_4, which opens great perspectives in designing novel and efficient Cu-based CO_2RR electrocatalysts.

■ ASSOCIATED CONTENT

Supporting Information

The Supporting Information is available free of charge at https://pubs.acs.org/doi/10.1021/jacs.0c11450.

Detailed information regarding the characterization analysis and electrochemical measurement (PDF)

Movie S1, dynamic simulation of $\{Cu_8\}$ (MP4)

Accession Codes

CCDC 2025580−2025581 contain the supplementary crystallographic data for this paper. These data can be obtained free of charge via www.ccdc.cam.ac.uk/data_request/cif, or by emailing data_request@ccdc.cam.ac.uk, or by contacting The Cambridge Crystallographic Data Centre, 12 Union Road, Cambridge CB2 1EZ, UK; fax: +44 1223 336033.

■ AUTHOR INFORMATION

Corresponding Author

Ya-Qian Lan − *Jiangsu Collaborative Innovation Centre of Biomedical Functional Materials, Jiangsu Key Laboratory of New Power Batteries, School of Chemistry and Materials Science, Nanjing Normal University, Nanjing 210023, P. R. China; School of Chemistry, South China Normal University, Guangzhou 510006, P. R. China;* orcid.org/0000-0002-2140-7980; Email: yqlan@njnu.edu.cn, yqlan@m.scnu.edu.cn

Authors

Lei Zhang − *Jiangsu Collaborative Innovation Centre of Biomedical Functional Materials, Jiangsu Key Laboratory of New Power Batteries, School of Chemistry and Materials Science, Nanjing Normal University, Nanjing 210023, P. R. China*

Xiao-Xin Li − *School of Chemistry and Chemical Engineering, Southeast University, Nanjing 211189, P. R. China*

Zhong-Ling Lang − *Key Laboratory of Polyoxometalate Science of the Ministry of Education, Faculty of Chemistry, Northeast Normal University, Changchun 130000, P. R. China;* orcid.org/0000-0002-8301-3629

Yang Liu − *Analysis and Testing Center, Tianjin University, Tianjin 300072, P. R. China*

Jiang Liu − *Jiangsu Collaborative Innovation Centre of Biomedical Functional Materials, Jiangsu Key Laboratory of New Power Batteries, School of Chemistry and Materials Science, Nanjing Normal University, Nanjing 210023, P. R. China*

Lin Yuan − *Jiangsu Collaborative Innovation Centre of Biomedical Functional Materials, Jiangsu Key Laboratory of New Power Batteries, School of Chemistry and Materials Science, Nanjing Normal University, Nanjing 210023, P. R. China*

Wan-Yue Lu − *Jiangsu Collaborative Innovation Centre of Biomedical Functional Materials, Jiangsu Key Laboratory of New Power Batteries, School of Chemistry and Materials Science, Nanjing Normal University, Nanjing 210023, P. R. China*

Yuan-Sheng Xia − *Jiangsu Collaborative Innovation Centre of Biomedical Functional Materials, Jiangsu Key Laboratory of New Power Batteries, School of Chemistry and Materials Science, Nanjing Normal University, Nanjing 210023, P. R. China*

Long-Zhang Dong − *Jiangsu Collaborative Innovation Centre of Biomedical Functional Materials, Jiangsu Key Laboratory of New Power Batteries, School of Chemistry and Materials Science, Nanjing Normal University, Nanjing 210023, P. R. China;* orcid.org/0000-0002-9276-5101

Da-Qiang Yuan − *State Key Laboratory of Structural Chemistry, Fujian Institute of Research on the Structure of Matter, Chinese Academy of Sciences, Fuzhou 350002, P. R. China;* orcid.org/0000-0003-4627-072X

Complete contact information is available at: https://pubs.acs.org/10.1021/jacs.0c11450

Author Contributions

[+]L. Z., X.-X. L., and Z.-L. L. contributed equally to this work.

Notes

The authors declare no competing financial interest.

■ ACKNOWLEDGMENTS

This work was financially supported by NSFC (Grant Nos. 21871141, 21871142, 92061101, 21901122, and 21901035), the Foundation of Jilin Educational Committee (Grant No. JJKH20190268KJ), the project funded by China Postdoctoral Science Foundation (Grant Nos. 2018M630572 and 2019M651873), the Priority Academic Program Development of Jiangsu Higher Education Institutions, and the Foundation of Jiangsu Collaborative Innovation Center of Biomedical Functional Materials. We also thank the staff from BL17B beamline of the National Facility for Protein Science Shanghai (NFPS) at Shanghai Synchrotron Radiation Facility for assistance during data collection.

■ REFERENCES

(1) Olah, G. A.; Prakash, G. K. S.; Goeppert, A. Anthropogenic chemical carbon cycle for a sustainable future. *J. Am. Chem. Soc.* **2011**, *133*, 12881−12898.

(2) He, M.; Sun, Y.; Han, B. Green carbon science: scientific basis for integrating carbon resource processing, utilization, and recycling. *Angew. Chem., Int. Ed.* **2013**, *52*, 9620−9633.

(3) Birdja, Y. Y.; Pérez-Gallent, E.; Figueiredo, M. C.; Göttle, A. J.; Calle-Vallejo, F.; Koper, M. T. M. Advances and challenges in understanding the electrocatalytic conversion of carbon dioxide to fuels. *Nat. Energy* **2019**, *4*, 732−745.

(4) Huang, Q.; Li, Q.; Liu, J.; Wang, Y.-R.; Wang, R.; Dong, L.-Z.; Xia, Y.-H.; Wang, J.-L.; Lan, Y.-Q. Disclosing CO_2 Activation Mechanism by Hydroxyl-Induced Crystalline Structure Transformation in Electrocatalytic Process. *Matter* **2019**, *1*, 1656−1668.

(5) Yang, H. B.; Hung, S.-F.; Liu, S.; Yuan, K.; Miao, S.; Zhang, L.; Huang, X.; Wang, H.-Y.; Cai, W.; Chen, R.; Gao, J.; Yang, X.; Chen, W.; Huang, Y.; Chen, H.-M.; Li, C.-M.; Zhang, T.; Liu, B. Atomically dispersed Ni(i) as the active site for electrochemical CO_2 reduction. *Nat. Energy.* **2018**, *3*, 140−147.
(6) Wang, L.; Chen, L.; Zhang, D.; Du, Y.; Amal, R.; Qiao, S.; Wu, J.; Yin, Z. Surface strategies for catalytic CO_2 reduction: from two-dimensional materials to nanoclusters to single atoms. *Chem. Soc. Rev.* **2019**, *48*, 5310−5349.
(7) Liu, S.; Yang, H.; Huang, X.; Liu, L.; Cai, W.; Gao, J.; Li, X.; Zhang, T.; Huang, Y.; Liu, B. Identifying Active Sites of Nitrogen-Doped Carbon Materials for the CO_2 Reduction Reaction. *Adv. Funct. Mater.* **2018**, *28*, 1800499.
(8) Qiu, Y.-L.; Zhong, H.-X.; Zhang, T.-T.; Xu, W.-B.; Li, X.-F.; Zhang, H.-M. Copper Electrode Fabricated via Pulse Electrodeposition: Toward High Methane Selectivity and Activity for CO_2 Electroreduction. *ACS Catal.* **2017**, *7*, 6302−6310.
(9) Hu, Q.; Han, Z.; Wang, X.; Li, G.; Wang, Z.; Huang, X.; Yang, H.; Ren, X.; Zhang, Q.; Liu, J.; He, C. Facile Synthesis of Sub-Nanometric Copper Clusters by Double Confinement Enables Selective Reduction of Carbon Dioxide to Methane. *Angew. Chem., Int. Ed.* **2020**, *59*, 19054−19059.
(10) Wang, Y.; Chen, J.; Wang, G.; Li, Y.; Wen, Z. Perfluorinated Covalent Triazine Framework Derived Hybrids for the Highly Selective Electroconversion of Carbon Dioxide into Methane. *Angew. Chem., Int. Ed.* **2018**, *57*, 13120−13124.
(11) Dinh, C.-T.; Burdyny, T.; Kibria, M. G.; Seifitokaldani, A.; Gabardo, C. M.; Garcia de Arquer, F. P.; Kiani, A.; Edwards, J. P.; De Luna, P.; Bushuyev, O. S.; Zou, C.; Quintero-Bermudez, R.; Pang, Y.; Sinton, D.; Sargent, E. H. CO_2 electroreduction to ethylene via hydroxide-mediated copper catalysis at an abrupt interface. *Science* **2018**, *360*, 783−787.
(12) Ma, W.; Xie, S.; Liu, T.; Fan, Q.; Ye, J.; Sun, F.; Jiang, Z.; Zhang, Q.; Cheng, J.; Wang, Y. Electrocatalytic reduction of CO_2 to ethylene and ethanol through hydrogen-assisted C−C coupling over fluorine-modified copper. *Nature Catalysis* **2020**, *3*, 478−487.
(13) Zhuang, T.-T.; Liang, Z.-Q.; Seifitokaldani, A.; Li, Y.; De Luna, P.; Burdyny, T.; Che, F.; Meng, F.; Min, Y.; Quintero-Bermudez, R.; Dinh, C. T.; Pang, Y.; Zhong, M.; Zhang, B.; Li, J.; Chen, P.-N.; Zheng, X.-L.; Liang, H.; Ge, W.-N.; Ye, B.-J.; Sinton, D.; Yu, S.-H.; Sargent, E. H. Steering post-C−C coupling selectivity enables high efficiency electroreduction of carbon dioxide to multi-carbon alcohols. *Nature Catalysis* **2018**, *1*, 421−428.
(14) Wang, Y.; Wang, Z.; Dinh, C.-T.; Li, J.; Ozden, A.; Golam Kibria, M.; Seifitokaldani, A.; Tan, C.-S.; Gabardo, C. M.; Luo, M.; Zhou, H.; Li, F.; Lum, Y.; McCallum, C.; Xu, Y.; Liu, M.; Proppe, A.; Johnston, A.; Todorovic, P.; Zhuang, T.-T.; Sinton, D.; Kelley, S. O.; Sargent, E. H. Catalyst synthesis under CO_2 electroreduction favours faceting and promotes renewable fuels electrosynthesis. *Nat. Catal.* **2020**, *3*, 98−106.
(15) Nitopi, S.; Bertheussen, E.; Scott, S. B.; Liu, X.; Engstfeld, A. K.; Horch, S.; Seger, B.; Stephens, I. E. L.; Chan, K.; Hahn, C.; Nørskov, J. K.; Jaramillo, T. F.; Chorkendorff, I. Progress and Perspectives of Electrochemical CO_2 Reduction on Copper in Aqueous Electrolyte. *Chem. Rev.* **2019**, *119*, 7610−7672.
(16) Xie, H.; Wang, T.; Liang, J.; Li, Q.; Sun, S. Cu-based nanocatalysts for electrochemical reduction of CO_2. *Nano Today* **2018**, *21*, 41−54.
(17) Gao, D.; Aran-Ais, R. M.; Jeon, H. S.; Roldan Cuenya, B. Rational catalyst and electrolyte design for CO_2 electroreduction towards multicarbon products. *Nat. Catal.* **2019**, *2*, 198−210.
(18) Garcia de Arquer, F. P.; Dinh, C.-T.; Ozden, A.; Wicks, J.; McCallum, C.; Kirmani, A. R.; Nam, D.-H.; Gabardo, C.; Seifitokaldani, A.; Wang, X.; Li, Y. C.; Li, F.; Edwards, J.; Richter, L. J.; Thorpe, S. J.; Sinton, D.; Sargent, E. H. CO_2 electrolysis to multicarbon products at activities greater than 1 A cm^{-2}. *Science* **2020**, *367*, 661−666.
(19) Aran-Ais, R. M.; Scholten, F.; Kunze, S.; Rizo, R.; Roldan Cuenya, B. The role of in situ generated morphological motifs and Cu(I) species in C_{2+} product selectivity during CO_2 pulsed electroreduction. *Nat. Energy* **2020**, *5*, 317−325.
(20) Li, F.; Li, Y. C.; Wang, Z.; Li, J.; Nam, D.-H.; Lum, Y.; Luo, M.; Wang, X.; Ozden, A.; Hung, S.-F.; Chen, B.; Wang, Y.; Wicks, J.; Xu, Y.; Li, Y.; Gabardo, C. M.; Dinh, C.-T.; Wang, Y.; Zhuang, T.-T.; Sinton, D.; Sargent, E. H. Cooperative CO_2-to-ethanol conversion via enriched intermediates at molecule−metal catalyst interfaces. *Nat. Catal.* **2020**, *3*, 75−82.
(21) Kuhl, K. P.; Cave, E. R.; Abram, D. N.; Jaramillo, T. F. New insights into the electrochemical reduction of carbon dioxide on metallic copper surfaces. *Energy Environ. Sci.* **2012**, *5*, 7050−7059.
(22) De Gregorio, G. L.; Burdyny, T.; Loiudice, A.; Iyengar, P.; Smith, W. A.; Buonsanti, R. Facet-Dependent Selectivity of Cu Catalysts in Electrochemical CO_2 Reduction at Commercially Viable Current Densities. *ACS Catal.* **2020**, *10*, 4854−4862.
(23) Li, Y.; Cui, F.; Ross, M. B.; Kim, D.; Sun, Y.; Yang, P. Structure-Sensitive CO_2 Electroreduction to Hydrocarbons on Ultrathin 5-fold Twinned Copper Nanowires. *Nano Lett.* **2017**, *17*, 1312−1317.
(24) Liu, S.; Huang, S. Size effects and active sites of Cu nanoparticle catalysts for CO2 electroreduction. *Appl. Surf. Sci.* **2019**, *475*, 20−27.
(25) Lin, S.-C.; Chang, C.-C.; Chiu, S.-Y.; Pai, H.-T.; Liao, T.-Y.; Hsu, C.-S.; Chiang, W.-H.; Tsai, M.-K.; Chen, H. M. Operando time-resolved X-ray absorption spectroscopy reveals the chemical nature enabling highly selective CO2 reduction. *Nat. Commun.* **2020**, *11*, 3525.
(26) Chen, K.; Ling, J.-L.; Wu, C.-D. In Situ Generation and Stabilization of Accessible Cu/Cu_2O Heterojunctions inside Organic Frameworks for Highly Efficient Catalysis. *Angew. Chem., Int. Ed.* **2020**, *59*, 1925−1931.
(27) Morales-Guio, C. G.; Cave, E. R.; Nitopi, S. A.; Feaster, J. T.; Wang, L.; Kuhl, K. P.; Jackson, A.; Johnson, N. C.; Abram, D. N.; Hatsukade, T.; Hahn, C.; Jaramillo, T. F. Improved CO_2 reduction activity towards C_{2+} alcohols on a tandem gold on copper electrocatalyst. *Nature Catalysis* **2018**, *1*, 764−771.
(28) Jiang, K.; Sandberg, R. B.; Akey, A. J.; Liu, X.; Bell, D. C.; Nørskov, J. K.; Chan, K.; Wang, H. Metal ion cycling of Cu foil for selective C−C coupling in electrochemical CO_2 reduction. *Nature Catalysis* **2018**, *1*, 111−119.
(29) Tan, X.; Yu, C.; Zhao, C.; Huang, H.; Yao, X.; Han, X.; Guo, W.; Cui, S.; Huang, H.; Qiu, J. Restructuring of Cu_2O to Cu_2O@Cu-Metal−Organic Frameworks for Selective Electrochemical Reduction of CO_2. *ACS Appl. Mater. Interfaces* **2019**, *11*, 9904−9910.
(30) Ren, D.; Deng, Y.; Handoko, A. D.; Chen, C. S.; Malkhandi, S.; Yeo, B. S. Selective Electrochemical Reduction of Carbon Dioxide to Ethylene and Ethanol on Copper(I) Oxide Catalysts. *ACS Catal.* **2015**, *5*, 2814−2821.
(31) Zhou, Y.; Che, F.; Liu, M.; Zou, C.; Liang, Z.; De Luna, P.; Yuan, H.; Li, J.; Wang, Z.; Xie, H.; Li, H.; Chen, P.; Bladt, E.; Quintero-Bermudez, R.; Sham, T.-K.; Bals, S.; Hofkens, J.; Sinton, D.; Chen, G.; Sargent, E. H. Dopant-induced electro localization drives CO_2 reduction to C_2 hydrocarbons. *Nat. Chem.* **2018**, *10*, 974−980.
(32) Andris, E.; Andrikopoulos, P. C.; Schulz, J.; Turek, J.; Ruzicka, A.; Roithova, J.; Rulisek, L. Aurophilic Interactions in [(L)AuCl]···[(L′)AuCl] Dimers: Calibration by Experiment and Theory. *J. Am. Chem. Soc.* **2018**, *140*, 2316−2325.
(33) Harisomayajula, N. V. S.; Makovetskyi, S.; Tsai, Y.-C. Cuprophilic Interactions in and between Molecular Entities. *Chem. - Eur. J.* **2019**, *25*, 8936−8954.
(34) He, Y.; Li, B.; O'Keeffe, M.; Chen, B. Multifunctional metal-organic frameworks constructed from meta-benzenedicarboxylate units. *Chem. Soc. Rev.* **2014**, *43*, 5618−5656.
(35) Lin, Z.-J.; Lü, J.; Hong, M.; Cao, R. Metal-organic frameworks based on flexible ligands (FL-MOFs): structures and applications. *Chem. Soc. Rev.* **2014**, *43*, 5867−5895.
(36) Wang, Y. R.; Huang, Q.; He, C.-T.; Chen, Y.; Liu, J.; Shen, F.-C.; Lan, Y.-Q. Oriented electron transmission in polyoxometalate-metalloporphyrin organic framework for highly selective electroreduction of CO_2. *Nat. Commun.* **2018**, *9*, 4466.

https://dx.doi.org/10.1021/jacs.0c11450
J. Am. Chem. Soc. XXXX, XXX, XXX−XXX

(37) Xin, Z.; Wang, Y.-R.; Chen, Y.; Li, W.-L.; Dong, L.-Z.; Lan, Y.-Q. Metallocene implanted metalloporphyrin organic framework for highly selective CO_2 electroreduction. *Nano Energy* **2020**, *67*, 104233.
(38) Dong, L.-Z.; Zhang, L.; Liu, J.; Huang, Q.; Lu, M.; Ji, W.-X.; Lan, Y.-Q. Stable Heterometallic Cluster-Based Organic Frameworks Catalysts for Artificial Photosynthesis. *Angew. Chem., Int. Ed.* **2020**, *59*, 2659−2663.
(39) Wang, X.-L.; Dong, L.-Z.; Qiao, M.; Tang, Y.-J.; Liu, J.; Li, Y.; Li, S.-L.; Su, J.-X.; Lan, Y.-Q. Exploring the Performance Improvement of Oxygen Evolution Reaction in Stable Bimetal-Organic Framework System. *Angew. Chem., Int. Ed.* **2018**, *57*, 9660−9664.
(40) Liu, S.; Yang, H. B.; Hung, S.-F.; Ding, J.; Cai, W.; Liu, L.; Gao, J.; Li, X.; Ren, X.; Kuang, Z.; Huang, Y.; Zhang, T.; Liu, B. Elucidating the Electrocatalytic CO_2 Reduction Reaction over a Model Single-Atom Nickel Catalyst. *Angew. Chem., Int. Ed.* **2020**, *59*, 798−802.
(41) Lu, X.-F.; Liao, P.-Q.; Wang, J.-W.; Wu, J.-X.; Chen, X.-W.; He, C.-T.; Zhang, J.-P.; Li, G.-R.; Chen, X.-M. An Alkaline-Stable, Metal Hydroxide Mimicking Metal−Organic Framework for Efficient Electrocatalytic Oxygen Evolution. *J. Am. Chem. Soc.* **2016**, *138*, 8336−8339.
(42) Wang, K.; Lv, X.-L.; Feng, D.; Li, J.; Chen, S.; Sun, J.; Song, L.; Xie, Y.; Li, J.-R.; Zhou, H.-C. Pyrazolate-Based Porphyrinic Metal−Organic Framework with Extraordinary Base-Resistance. *J. Am. Chem. Soc.* **2016**, *138*, 914−919.
(43) Li, X.-X.; Liu, J.; Zhang, L.; Dong, L.-Z.; Xin, Z.-F.; Li, S.-L.; Huang-Fu, X.-Q.; Huang, K.; Lan, Y.-Q. Hydrophobic Polyoxometalate-Based Metal-Organic Framework for Efficient CO_2 Photoconversion. *ACS Appl. Mater. Interfaces* **2019**, *11*, 25790−25795.
(44) Park, K. S.; Ni, Z.; Cote, A. P.; Choi, J. Y.; Huang, R.; Uribe-Romo, F. J.; Chae, H. K.; O'Keeffe, M.; Yaghi, O. M. Exceptional chemical and thermal stability of zeolitic imidazolate frameworks. *Proc. Natl. Acad. Sci. U. S. A.* **2006**, *103*, 10186−10191.
(45) Zhong, H.; Ghorbani-Asl, M.; Ly, K. H.; Zhang, J.; Ge, J.; Wang, M.; Liao, Z.; Makarov, D.; Zschech, E.; Brunner, E.; Weidinger, I. M.; Zhang, J.; Krasheninnikov, A. V.; Kaskel, S.; Dong, R.; Feng, X. Synergistic electroreduction of carbon dioxide to carbon monoxide on bimetallic layered conjugated metal-organic frameworks. *Nat. Commun.* **2020**, *11*, 1409.
(46) Matheu, R.; Gutierrez-Puebla, E.; Monge, M. Á.; Diercks, C. S.; Kang, J.; Prévot, M. S.; Pei, X.; Hanikel, N.; Zhang, B.; Yang, P.; Yaghi, O. M. Three-Dimensional Phthalocyanine Metal-Catecholates for High Electrochemical Carbon Dioxide Reduction. *J. Am. Chem. Soc.* **2019**, *141*, 17081−17085.
(47) Zhang, X.; Zhang, Y.; Li, Q.; Zhou, X.; Li, Q.; Yi, J.; Liu, Y.; Zhang, J. Highly efficient and durable aqueous electrocatalytic reduction of CO_2 to HCOOH with a novel bismuth−MOF: experimental and DFT studies. *J. Mater. Chem. A* **2020**, *8*, 9776−9787.
(48) Lei, F.; Liu, W.; Sun, Y.; Xu, J.; Liu, K.; Liang, L.; Yao, T.; Pan, B.; Wei, S.; Xie, Y. Metallic tin quantum sheets confined in graphene toward highefficiency carbon dioxide electroreduction. *Nat. Commun.* **2016**, *7*, 12697.
(49) Chen, S.; Su, Y.; Deng, P.; Qi, R.; Zhu, J.; Chen, J.; Wang, Z.; Zhou, L.; Guo, X.; Xia, B. Y. Highly Selective Carbon Dioxide Electroreduction on Structure-Evolved Copper Perovskite Oxide toward Methane Production. *ACS Catal.* **2020**, *10*, 4640−4646.
(50) Manthiram, K.; Beberwyck, B. J.; Alivisatos, A. P. Enhanced Electrochemical Methanation of Carbon Dioxide with a Dispersible Nanoscale Copper Catalyst. *J. Am. Chem. Soc.* **2014**, *136*, 13319−13325.
(51) Weng, Z.; Wu, Y.; Wang, M.; Jiang, J.; Yang, K.; Huo, S.; Wang, X.-F.; Ma, Q.; Brudvig, G. W.; Batista, V. S.; Liang, Y.; Feng, Z.; Wang, H. Active sites of copper-complex catalytic materials for electrochemical carbon dioxide reduction. *Nat. Commun.* **2018**, *9*, 415.
(52) Wang, Y.; Chen, Z.; Han, P.; Du, Y.; Gu, Z.; Xu, X.; Zheng, G. Single-Atomic Cu with Multiple Oxygen Vacancies on Ceria for Electrocatalytic CO_2 Reduction to CH_4. *ACS Catal.* **2018**, *8*, 7113−7119.
(53) Varela, A. S.; Ju, W.; Reier, T.; Strasser, P. Tuning the Catalytic Activity and Selectivity of Cu for CO_2 Electroreduction in the Presence of Halides. *ACS Catal.* **2016**, *6*, 2136−2144.
(54) Nam, D.-H.; Shekhah, O.; Lee, G.; Mallick, A.; Jiang, H.; Li, F.; Chen, B.; Wicks, J.; Eddaoudi, M.; Sargent, E. H. Intermediate Binding Control Using Metal−Organic Frameworks Enhances Electrochemical CO_2 Reduction. *J. Am. Chem. Soc.* **2020**, *142*, 21513−21521.
(55) Bodappa, N.; Su, M.; Zhao, Y.; Le, J.-B.; Yang, W.-M.; Radjenovic, P.; Dong, J.-C.; Cheng, J.; Tian, Z.-Q.; Li, J.-F. Early Stages of Electrochemical Oxidation of Cu(111) and Polycrystalline Cu Surfaces Revealed by *in Situ* Raman Spectroscopy. *J. Am. Chem. Soc.* **2019**, *141*, 12192−12196.
(56) Zhang, W.; Huang, C.; Xiao, Q.; Yu, L.; Shuai, L.; An, P.; Zhang, J.; Qiu, M.; Ren, Z.; Yu, Y. Atypical Oxygen-Bearing Copper Boosts Ethylene Selectivity toward Electrocatalytic CO_2 Reduction. *J. Am. Chem. Soc.* **2020**, *142*, 11417−11427.
(57) Zhao, Y.; Truhlar, D. G. The M06 suite of density functionals for main group thermochemistry, thermochemical kinetics, noncovalent interactions, excited states, and transition elements: two new functionals and systematic testing of four M06-class functionals and 12 other functionals. *Theor. Chem. Acc.* **2008**, *120*, 215−241.
(58) Hay, P. J.; Wadt, W. R. Ab initio effective core potentials for molecular calculations—potentials for K to Au including the outermost core orbitals. *J. Chem. Phys.* **1985**, *82*, 299−310.
(59) Ditchfield, R.; Hehre, W. J.; Pople, J. A. Self-consistent molecular-orbital methods. IX. An extended Gaussian-type basis for molecular-orbital studies of organic molecules. *J. Chem. Phys.* **1971**, *54*, 724−728.
(60) Tomasi, J.; Mennucci, B.; Cammi, R. Quantum mechanical continuum solvation models. *Chem. Rev.* **2005**, *105*, 2999−3094.
(61) Bader, R. F. W. *Atoms in Molecules: Quantum Theory*; Oxford University Press: Oxford, U.K., 1990.

https://dx.doi.org/10.1021/jacs.0c11450
J. Am. Chem. Soc. XXXX, XXX, XXX−XXX